Lithographically Fabricated Planar Holographic Bragg Reflectors

C. Greiner, *Member, IEEE, Member, OSA*, D. Iazikov, *Member, IEEE*, and T. W. Mossberg, *Member, IEEE, Fellow, OSA*

***Abstract*—Planar holographic Bragg reflectors (HBRs) are computer-generated slab-waveguide holograms. They operate in two dimensions to provide powerful free-space-like spectral and spatial processing of optical signals in an integrated optics environment. An HBR typically images an input port to an output port while applying a specific spectral filtering function. HBRs are fully consistent with robust photolithographic or imprint-based fabrication and can be flexibly designed to offer a wide range of spatial wavefront control and single and multichannel spectral transfer functions. We report on lithographically fabricated, focusing HBRs implemented in the silica-on-silicon format whose spectral and spatial performances reach fundamental device limits set, respectively, by Fourier transform and diffractive constraints. We also demonstrate that HBRs support a unique process-friendly approach to apodization and overlay that uses fixed-depth etching and partial contour writing to achieve continuous reflective amplitude control of constitutive diffractive elements.**

***Index Terms*—Bragg reflectors, filtering, grating, integrated optics, integrated photonic circuits, multiplexing, photonic crystals, planar lightwave circuit, slab waveguide, volume holography.**

I. Introduction

RECENTLY, a new class of in-plane volume holographic devices, planar holographic Bragg reflectors (HBRs), was proposed [1], [2], and demonstrated [3]. HBRs consist of computer-generated, two-dimensional (2-D), etched gratings operative on optical signals propagating entirely within a slab waveguide. In the slab waveguide, light can propagate without constraints in two dimensions—a geometry that allows 2-D Bragg structures to provide powerful spectral and spatial holographic functions. A single HBR can simultaneously spatially image an input signal to an output port (or one point within an integrated optical circuit to another) while at the same time providing spectral filtering of the signal. Unlike fiber and channel-waveguide gratings [4]–[9], where separation of the counter-propagating input and output signals typically requires a bulky circulator or a lossy power splitter, planar HBRs provide spatially distinct and thus easily accessed outputs.

Since they are planar-based structures, HBRs can be fabricated by photolithography or low-cost mass production nanoreplication techniques such as hot embossing [10]–[12] or nanoimprint lithography [13]. In contrast to UV-written grating structures, photolithographic structures can be written with complete amplitude, phase, and geometric control over individual diffractive elements. Precise control of HBR diffractive element reflective strength and relative phase as a function of position provides the powerful ability to implement arbitrary phase-coherent spectral filtering functions.

In the limit of weak reflectivity, the reflection spectrum of an HBR is simply related to the spatial Fourier transform of its effective reflection coefficient expressed as a function of optical depth into the device [1]. In the limit of strong reflectivity, the relationship of local reflective amplitude and phase to the spectral transfer function is more complex, but the ability to implement broad ranges of filtering functions remains. Tailoring of device spectral filtering functions has been recently demonstrated for fiber Bragg gratings [4]–[7], [14]–[17] and channel-waveguides [8], [9], [18] by a variety of techniques. However, methods demonstrated do not provide for line-by-line control of diffractive element amplitude and phase. Photolithographically fabricated HBRs are compatible with line-by-line amplitude and phase apodization as discussed later.

In principle, HBRs provide a path to unique optical circuits that operate entirely without wire-analog channel waveguides, being based on HBR-mediated signal transport where signals freely overlap as they are imaged from active element to active element. HBRs provide the power of free-space optics in a fully integrated environment. The powerful volume-holographic approach allows HBR structures, via computer-generated complex-shaped diffractive contours, to provide fully optimized spatial mapping of the complex field distribution of an arbitrary input field mode to the complex field distribution of a different output field mode. This broad in-plane spatial wavefront transformation capability contrasts with previously discussed 2-D distributed Bragg reflectors intended for out-of-plane applications such as laser feedback and outcoupling [19]–[21] and free-space to slab-waveguide beam coupling [22], [23]. The aforementioned holographic imaging function made possible by HBRs is generally more powerful than that provided by simple confocal elliptical DBRs previously discussed in the context of spectral multiplexing [24], [25]. While ellipses map one point to another point, their focusing power degrades when input and output optics deviate from the point source limit. In many useful cases, input/output coupling requires explicit integration of the nonsingular nature of the real fields employed. Computer-generated holographic nonconic diffractive contours can map real input ports to real output ports with great precision and hence low loss.

II. HBR Architecture and Operational Principles

Fig. 1(a) is a schematic HBR cross section. The devices described here consist of a silica slab waveguide with a central

Manuscript received June 27, 2003; revised August 14, 2003.

The authors are with LightSmyth Technologies, Inc., Eugene, OR 97041 USA (e-mail: cgreiner@lightsmyth.com).

Digital Object Identifier 10.1109/JLT.2003.822147

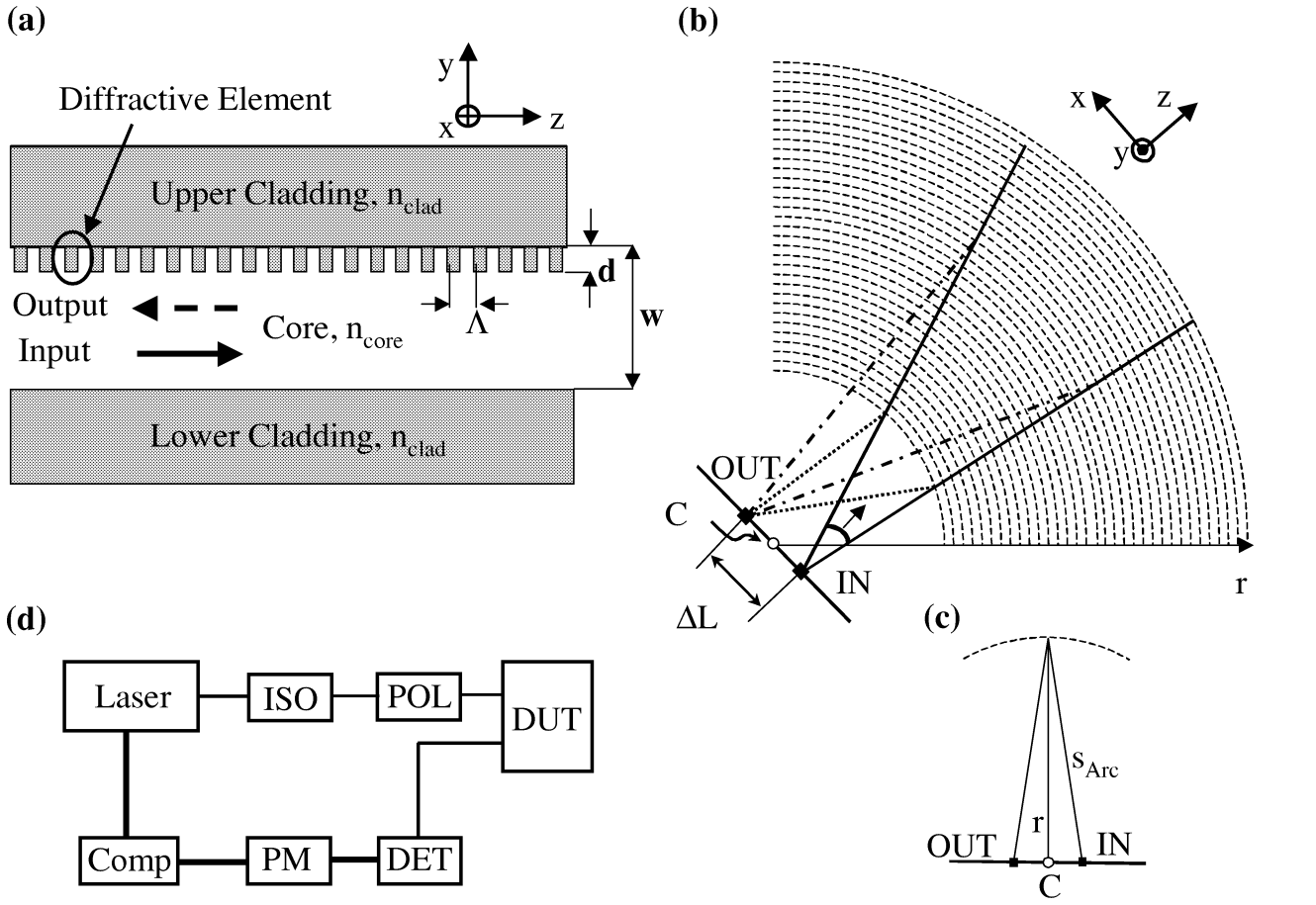

Fig. 1. Planar Holographic Bragg Reflector Schematics. (a) Cross-sectional view; w, waveguide width; d, grating depth; Λ, grating period; $\mathrm{n_{core}}$ ($\mathrm{n_{clad}}$), core (cladding) refractive index. (b) Top view; IN (OUT), input (output) port; $\Delta\mathrm{L}$, input/output port separation; C, center of curvature of diffractive contours. (c) Schematic illustrating the relation between device radial depth, r, and optical path, $\mathrm{s_{Arc}}$, to a given diffractive arc. (d) Test setup; ISO, optical isolator; POL, polarization controller; DUT, device under test; DET, detector; PM power meter; Comp, Computer.

core of thickness $\mathrm{w} \approx 6\,\mu$m and bilateral 15-$\mu$m-thick cladding layers mounted on a silicon wafer. The core index, $\mathrm{n_{core}} \approx 1.46$ and the core-cladding index differential, $\Delta \approx 0.8\%$. Fig. 1(a) shows lithographically scribed diffractive contours located at the upper core-cladding interface. The diffractive contours, with depth, $\mathrm{d} \approx 450\,\mathrm{nm}$, consist of trenches filled with cladding material. For an HBR operating in mth-order, diffractive elements are spaced approximately by a distance $\Lambda = \mathrm{m} \times \lambda/2\mathrm{n_{eff}}$ ($\mathrm{m} = 1, 2, 3\ldots$), where λ is the vacuum wavelength of the resonant light and $\mathrm{n_{eff}}$ is the effective refractive index of the slab waveguide.

Fig. 1(b) is a schematic top view of a planar HBR. Dashed lines correspond to diffractive contours. Each diffractive contour acts as an imaging device mapping the input port onto the output port. In optimized designs, the contour profile is chosen to optimally project the input field wavefronts onto those of an output port eigenmode like a custom aspheric mirror specially designed for a specific device geometry. The input signal is coupled into the device via the input port IN and expands in the slab region prior to interacting with the diffractive contours. It is the coherent interaction of all the diffractive contours that controls the HBR spectral filtering function. In all devices reported on here, the diffractive contours are unoptimized circular arcs having a common center C. The radius of the first (last) diffractive contour is 2 mm (9 mm). There are $\sim$13 300/m diffractive contours, where m is the diffractive order. The maximal device width is 3 mm yielding a highly compact footprint of about 0.3 cm^2. Input and output ports are spatially separated by a distance $\Delta\mathrm{L}$ and symmetrically located about point C. We refer to the line containing input port, output port, and point C as input/output plane. Our use of circular structures in this initial work was predicated on their convenient modeling in simulations and consistency with core objectives which include characterizing fabrication limitations and effects of partial contour scribing on spatial focus. Computer-generated holographic contours will improve input-output coupling through optimization of spatial wavefront transformation, but should behave similarly in the presence of fabrication and partial scribing effects.

Adjacent HBR diffractive contours are spaced such that the optical path length $\mathrm{s_{Arc}}$ as shown in Fig. 1(c), is incremented by a constant amount $\Lambda = \mathrm{m} \times \lambda/2\mathrm{n_{eff}}$ from one diffractive contour to the next. Consequently, the spacing between adjacent diffractive contours, as measured along r [see Fig. 1(c)], is weakly chirped. The HBR will provide imaging between any input-output port pair symmetrically located about the point C, but the weak chirp introduced during design to equalize contour-to-contour optical path increments will function optimally only at the design port separation $\Delta\mathrm{L}$. In the present studies

$\Delta L = 400\ \mu$m. Unless otherwise noted all results shown were taken for this port separation.

For the measurements presented in this paper, input and output ports lie either in the interior or at the edge of the device die. In the former (latter) case, a fiber butt-coupled to a 6 μm channel waveguide (fiber butt-coupled to the die edge) is used to inject light into the slab region. The channel waveguides employed are adiabatically tapered to a final launch width of 12.7 μm and launch at an angle of 2.275° with respect to the normal to the input/output plane so that they are aimed toward the center of the HBR. The actual angular width (about point C) of diffractive contours fabricated varies from 0.53 rad for the first diffractive contour to 0.33 rad for the last diffractive contour. The wider opening angle at the input/output end accommodates the 200-μm offset of the input/output ports from the center of curvature. The minimum diffractive contour angular width seen from the input port is 0.3 rad. Approximately 99.8% of the input beam power passes within this angular range.

Fig. 1(d) shows a typical test setup. Light from a linearly polarized tunable laser is passed through an isolator and a polarization controller and injected into the HBR. The HBR output is detected by a photodetector followed by a power meter. For spectral-transfer-function measurements, the laser wavelength is stepped in small increments across the HBR resonance width. The purity of the linearly polarized input P_p/P_o where $P_p(P_o)$ is the power along (orthogonal to) the test direction, was ~650.

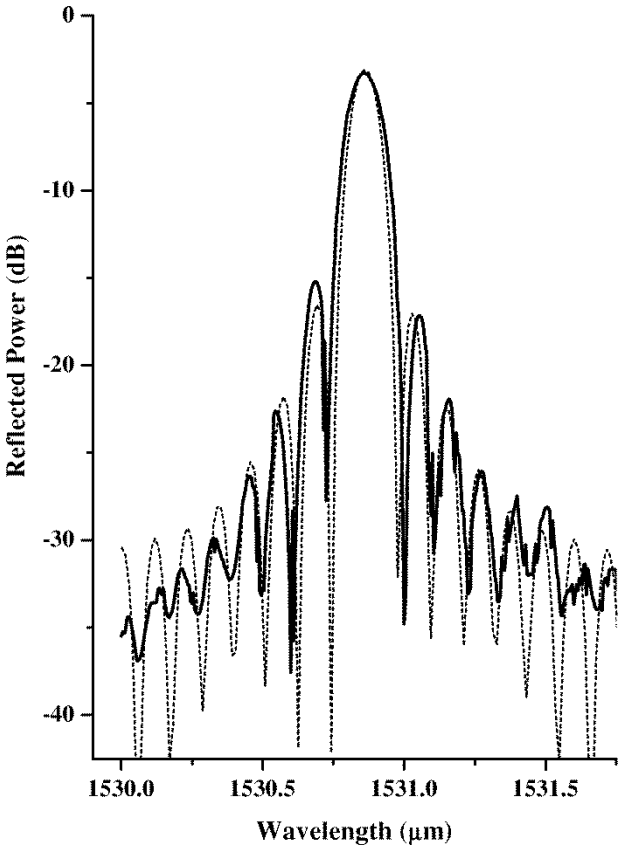

Fig. 2. Solid line, measured insertion loss versus wavelength for a 7-mm-long planar holographic Bragg reflector (TE polarization). Dashed line, spectral transfer function calculated by Huygens-Fresnel diffraction theory.

III. HBR Simulations and Measurements

A. Spectral and Spatial Output of a Simple HBR

In Fig. 2, we present (solid line) the measured insertion loss versus input wavelength of a first-order $(m = 1)$ planar HBR fabricated as above for the case of TE input polarization. The band center insertion loss of the device (excluding fiber-to-waveguide coupling losses) was 3.1 dB. The relatively low HBR reflectivity found in this case can be increased by, for example, lengthening the grating, reducing core thickness, increasing grating etch depth, increasing core-cladding index contrast, or placing the diffractive elements within the core. The fiber-to-slab-waveguide coupling loss was measured to be 1.4 dB making total device insertion loss 4.5 dB. The HBR used in this spectral measurement was designed for moderate reflectivity. Other HBRs have been fabricated whose intrinsic insertion loss has been measured to be less than 0.5 dB. As seen in Fig. 2, the 7-mm-long HBR has a spectral full-width at half maximum (FWHM) of ~0.13 nm, corresponding to a fractional spectral resolution $\Delta\lambda/\lambda$ better than 10^{-4}, close to the Fourier-transform-limited fractional bandpass of 7.5×10^{-5}, calculated for a 1-D grating with 13 305 grating lines. The result of Fig. 2 indicates that the lithographic fabrication process provides control at the same level of precision over imaging fidelity, feature placement, and index homogeneity over the device length. The accuracy of the measured center wavelength of $\sim 1.5308\ \mu$m as compared to the design value of 1.530 37 μm is better than 3×10^{-4} and attests to excellent control over recticle scale, stepper magnification, and waveguide refractive index. The design wavelength was based on cataloged refractive index and stepper magnification. Center wavelength predictability is substantially improved as the fabrication system is calibrated by actual device measurement.

Fig. 2, dashed line, is the modeled device spectral transfer function calculated using 2-D Huygens-Fresnel diffraction theory. An input field with Gaussian transverse distribution (1/e-diameter 12 μm), perfect waveguide index homogeneity, and perfect diffractive contour spacing were assumed. The agreement between modeled and measured response is excellent. The measured transfer function is slightly broader than that of the model. This is likely the result of input field depletion not taken into account in the model, which is fully valid only in the limit of weak reflectivity. The agreement between simulation and measured performance seen in Fig. 2 conclusively demonstrates that the silica-on-silicon format and submicron lithographic fabrication can provide fully coherent planar holographic structures of centimeter scale.

Fig. 3 shows the HBR spectral transfer function for port separations other than the design separation. The solid (dashed) lines in Fig. 3(a)–(c) show measured (simulated) insertion loss versus input wavelength for port separations $\Delta L = 0$ (retroreflection), 200, and 600 μm. Since the diffractive contour spacing is not designed for these separations and thus appears chirped, observed and calculated passbands are distorted and broadened relative to the passband found for $\Delta L = 400\ \mu$m. Also, the passband centers are slightly shifted from the design value and fairly high insertion loss is observed.

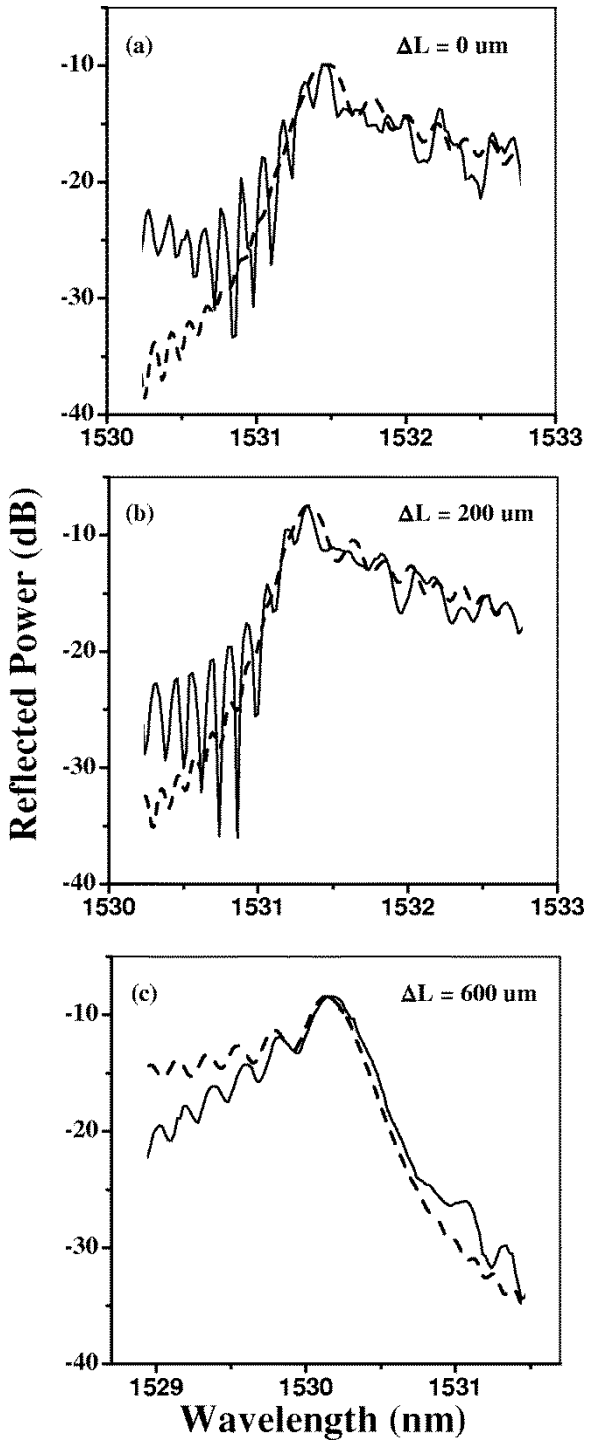

Fig. 3. (a)–(c) HBR spectral transfer function for port separations $\Delta L = 0\ \mu$m (retroreflection), 200 and 600 μm. Solid (dashed) lines, test data (modeled response).

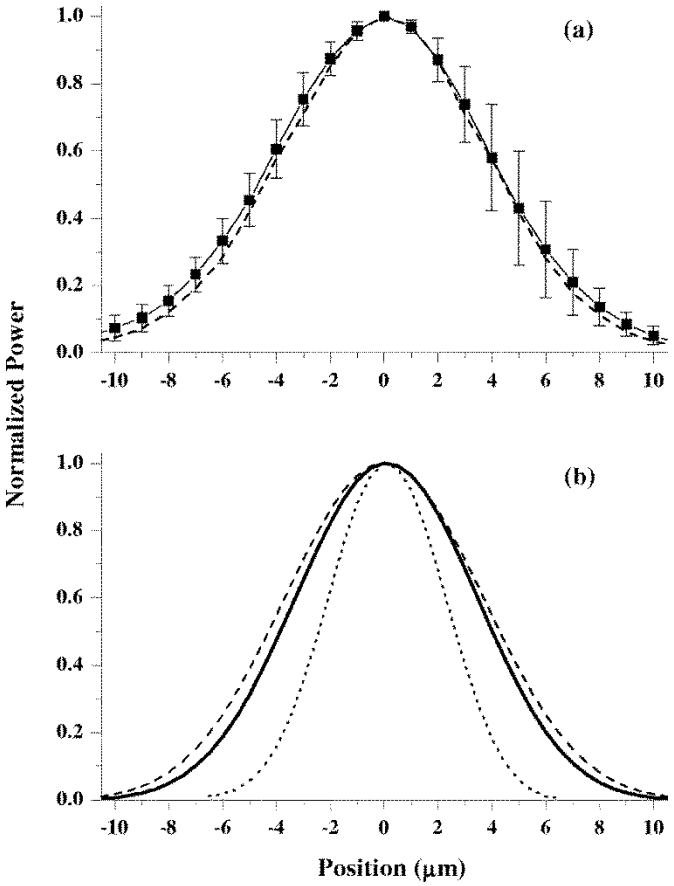

Fig. 4. Measured and calculated HBR output spatial profiles. (a) squares, HBR data; dashed line, measured input fiber spatial power profile. (b) solid line, calculated HBR spatial output profile; dashed line, calculated input spatial power profile; dotted line, calculated unconvolved HBR output profile.

In Fig. 4, we explore the focusing properties of the fabricated HBR. For these measurements, device die, without channel waveguides, are cut $(\pm 15\ \mu\text{m})$ so that the die edge contains the diffractive-contour center of curvature and both I/O ports. An SMF-28 fiber, used as input fiber, is positioned 200 μm to one side of the center of curvature. A second SMF-28 fiber, the collection fiber, is scanned parallel to the die edge throughout a region 200 μm to the opposite side of the center of curvature. The die and both fibers were square cut. The input (collection) fiber was oriented at an angle of 2° (0°) with respect to the normal to the die. Squares shown in Fig. 4(a) represent mean power coupled into the collection fiber as a function of collection-fiber position averaged over five output-profile measurements. The origin of the horizontal scale of Fig. 4(a) is set to coincide with the peak of the observed power distribution. The power peak coincided with the expected 200-μm displacement from the center of curvature to within measurement accuracy of a few μm. Error bars are standard deviations. Also shown, as a dashed line, is the power profile measured when the collection fiber is scanned directly across the face of the input fiber. From the measurement of Fig. 4(a), we conclude that the holographic Bragg reflector produces a focused output power profile closely approximating the device input power distribution.

In Fig. 4(b), we compare the measured output power profile with that expected on the basis of Huygens-Fresnel diffraction theory as applied to the HBR device structure. The input and collection fiber modes are modeled as a Gaussian with a 1/e-field diameter of 10.4 μm. The input field enters the HBR 200 μm to one side of the center of curvature. The HBR was modeled as a family of discrete point scatterers densely sampling the diffractive contours. The output field distribution is calculated by coherently adding the fields scattered by the family of HBR-representative points. The solid (dashed) line in Fig. 4(b), shows the calculated HBR output (model input) power profile con-

volved with the model collection power profile. The dotted line in Fig. 4(b) represents the unconvolved HBR output power profile. As can be seen, the calculated output power profile and the model input power profile are, after convolution, essentially identical to each other and the measurements of Fig. 4(a). This result agrees with the unity conjugate ratio expected on basis of simple imaging theory. The output power profile measured in Fig. 4(a) is essentially diffraction limited on the basis of perfect circular diffractive contours.

B. Effective Grayscale Apodization

Flexible design of HBR spectral transfer functions requires control over the reflective amplitude and phase of each of the diffractive contours [see Fig. 1(b)]. Relative reflective phase shifts over the range of $\pm\pi$ are provided by spatially displacing diffractive contours over a range $\pm\lambda/4\mathrm{n}_{\mathrm{eff}}$. Since HBR contours comprise a computer-generated hologram, which is laser (or e-beam) written onto a standard reticle and photolithographically scribed onto slab waveguides, full reflective phase control by controlled displacement is conveniently available. The reflective amplitude of a trench-like reflective element is determined by various factors such as trench depth, trench width, refractive index contrast between the core and fill materials, etc. While these factors may in principle be used to control the reflective amplitude of the diffractive contours, their practical implementation is inconsistent with typical lithographic practice that usually employs a common etch depth across each wafer, uses a single trench-fill material, and is subject to process-related trench width variations.

Fortunately, the 2-D nature of HBRs allows for unconventional yet powerful and lithographically friendly approaches to reflective amplitude control. Referring to Fig. 1(b) and considering monochromatic input light, one can see that a single diffractive contour k contributes, an amount to the output signal field given by

$$E_{out}^{k} \propto \int_{contour\ k} E_{in}(\vec{r})a_k(\vec{r}) \tag{1}$$

where $E_{in}(\vec{r})$ and $a_k(\vec{r})$ are, respectively, the input field and amplitude reflection coefficient at contour position $\vec{r}$. For simplicity, it is assumed that the HBR has been designed so that contributions to the output field from all locations on the single contour arrive with the same phase—a typical condition for effective imaging. Equation (1) implies that partial contour scribing (i.e., creating a trench along only selected portions of a diffractive contour) provides a means of continuously controlling the contour's contribution to the output field without the need for lithographically challenging variations in diffractive-contour trench morphology.

While the partial scribing approach to achieving continuous reflective amplitude control for individual diffractive contours is conceptually simple, certain details must be considered. In order to preserve the focusing character of the HBR, the partially written diffractive contours must generate substantially the same output wavefront as the fully written diffractive contours. The variation in input field amplitude along the contour must be either explicitly considered in determining which portions of a contour to fill, or a fill pattern must be adopted that is immune to a range of input field variations. Furthermore, correlation in fill pattern between successive diffractive contours must be considered to ensure that portions of the input field do not "leak" through holes in the HBR structure. Finally, since the effective waveguide refractive index is perturbed, albeit weakly, by the presence of diffractive element trenches, spatial variations in the effective index introduced by partial scribing must be explicitly accounted for in the HBR design process. We refer to the partial writing of diffractive contours in HBR devices as "effective grayscale."

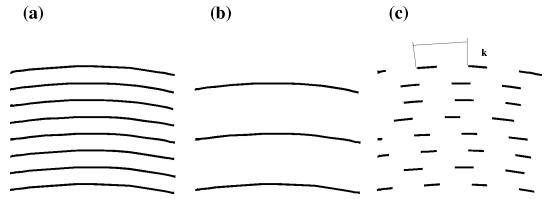

Fig. 5. Blow-up view of the diffractive contours of: (a) the fully scribed first-order, (b) third-order, and (c) partially scribed (0.33 grayscale) HBR.

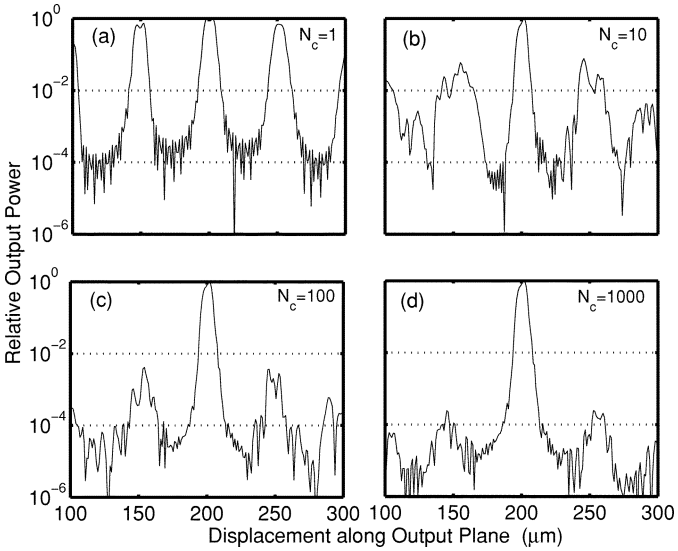

Fig. 6. Simulated output power as a function of position along the output plane for (a)–(d) 1, 10, 100, and 1000 partially written diffractive contours showing the decrease in sidelobe power with increasing contour count. The primary output image is located at 200 μm.

We have fabricated HBR structures to test certain aspects of the effective grayscale concept. We wish to compare HBRs written with a fixed 0.33 fraction of each contour scribed to HBRs having fully written contours regarding: 1) spatial focusing properties; 2) overall spectral transfer function; and 3) relative reflective strength. First- and third-order HBRs were fabricated with completely filled (i.e., scribed) diffractive contours. A second first-order HBR was partially scribed. Blow-ups of the diffractive contours of these HBRs are shown in schematically in Fig. 5(a)–(c), respectively. In the case of the partially written HBR, each contour was divided into 20 equal angular segments of angular width θ_{k}, and one-third of each angular segment was lithographically scribed to produce a trench. This is shown in Fig. 5(c), where the trenched regions (dark) occupy one-third of each contour. As aforementioned, and unlike the

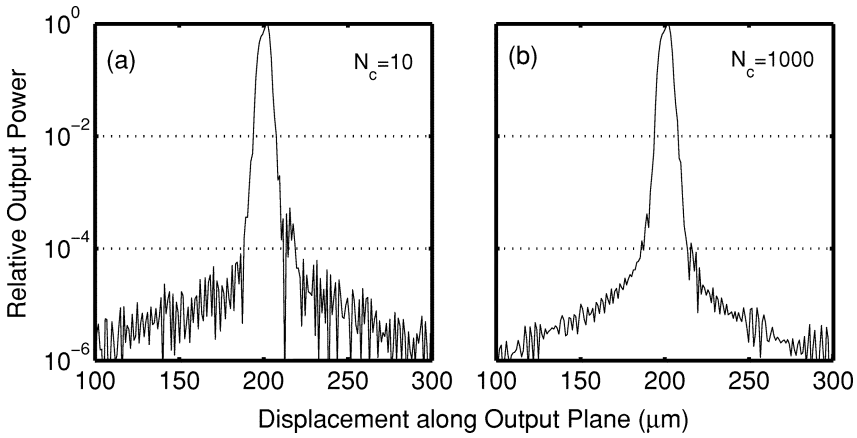

Fig. 7. Simulated output power as a function of position along output plane for (a) 10 and (b) 1000 fully written continuous diffractive contours. The primary output image is located at 200 μm.

simple HBR schematic of Fig. 1(b), diffractive contours of the actual HBRs subtend increasingly smaller angles as one moves away from the input/output plane. Owing to this variation in total angular width subtended by the diffractive contours, the angular segment width $\theta_{\rm k}$ ranges from 0.0165 to 0.0265 rad. The angular segments of successive diffractive elements were given random angle shifts of magnitude $\eta_{\rm k}\theta_{\rm k}$, where $\eta_{\rm k}$ is randomly generated from the interval (0,1) for each contour.

We first consider the imaging properties of HBRs implemented with effective grayscale (partial contour scribing). The division of each diffractive contour into 20 partially scribed segments provides for high fidelity sampling of the input signal beam. On the other hand, introduction of a noncontinuous, grating-like structure to the diffractive contour can in certain cases introduce ghost structures in the output plane. Theoretical simulation and HBR measurement reveal that ghosts structures are greatly suppressed in HBR structures with large numbers of diffractive contours by two implemented design factors, i.e., the random angular shifts described above and by the variation in angular segment size.

In Fig. 6, we show the calculated power as a function of position along the output plane of an HBR with partially scribed diffractive contours and various numbers $\rm N_c$ of diffractive contours. Except for Fig. 6(a) which depicts the power distribution produced by a single diffractive contour $(\rm N_c = 1)$ positioned in the middle of the fabricated structure, contours are distributed uniformly throughout the same physical region as the fabricated HBRs. Contour spacing and, hence, effective diffractive order are adjusted as necessary. Output plane powers shown are using diffraction theory and a dense point scatterer representation of the HBR as described earlier. The input port is positioned at -200 μm, the diffractive-element center of curvature at 0, which places the nominal output port location at $+200$ μm.

In Fig. 6(a), the power distribution created by a single partially written contour shows a primary image at $+200$ μm as well as sidelobes of nearly equal strength. The sidelobes correspond to diffractive orders of the segmented contour viewed as a reflective diffraction grating. The side lobes appear equally spaced about the primary image by a distance $\lambda/\sin\theta_{\rm k}$, where $\theta_{\rm k}$ is the angular segment width of the single written contour. In Fig. 6(b), an HBR with a total of 10 diffractive contours is analyzed. The sidelobes calculated are weaker and they appear broadened. The broadening effect arises from the variation in the magnitude of $\theta_{\rm k}$ within the HBR structure. The random angular shift between the scribing patterns of successive diffractive contours has the effect of introducing random phase changes onto the fields contributed by each contour to the sidelobes. These phase changes do not affect the primary image. Owing to the random phase shifts, the sidelobes should decrease in power relative to the primary image by a factor of approximately $1/\rm N_c$ (based on random-walk analysis). The variation in $\theta_{\rm k}$ and the random angular shifts together result in approximately one and a half orders of magnitude reduction in sidelobe power relative to the primary image (center peak) even when only 10 contours are written. In Fig. 6(c) and (d), the output plane power distribution for $\rm N_c = 100$ and $\rm N_c = 1000$ contours, respectively are displayed. The 1000-contour HBR has a simulated sidelobe reduction of approximately 4-orders of magnitude relative to the primary image. Simulation of the full 13 305-contour fabricated HBR was not performed owing to computational limitations.

In Fig. 7, we present simulations of HBRs comprised of fully written diffractive contours (no grayscale). The absence of sidelobes in Fig. 7, serves to confirm the introduction of grayscale partial scribing as the source of the sidelobes observed in Fig. 6.

Measurements of power versus position along the output plane were accomplished as above by scanning an SMF-28 fiber along a line parallel to the planar waveguide edge. In Fig. 8(a), we plot (solid line) output power versus position for a fully written first-order HBR with the input signal wavelength set to maximize HBR reflectivity. The dotted line at the bottom represents the scattered light background level as measured with the input laser tuned 20 nm above the HBR resonance wavelength. In correspondence with the simulations, the focused HBR output is centered at 200 μm, the diffractive-contour center of curvature is located at 0, and the input signal enters at -200 μm. The measured output power profile of Fig. 8(a) is in quite good agreement with the simulated power profile of Fig. 7(b) considering the background level. The minimum insertion loss for the measurement of Fig. 8(a) is $+3.8$ dB, which includes losses from fiber-to-planar-waveguide coupling. The solid line of Fig. 8(b) represents measured output power versus output plane position produced by a first-order

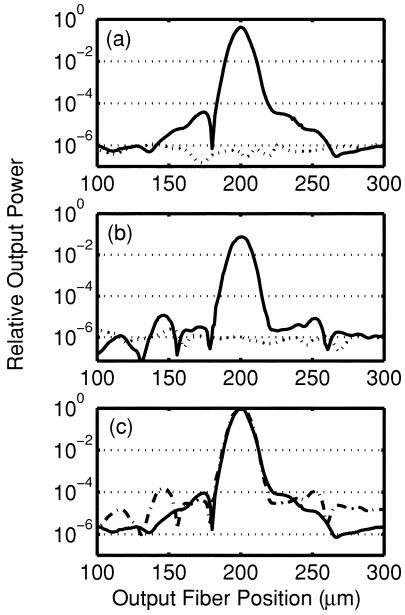

Fig. 8. Measured output power as a function of position along output plane for (a) fully written first-order HBR; (b) partially written (0.33 fraction) first-order HBR; (c) superimposed fully and partially written HBR measurements. The lower dotted line in (a) and (b) represents a background light power level corresponding primarily to input signal scattered off the square-cut die boundaries.

HBR with each diffractive contour written at the grayscale level of 0.33. As in Fig. 8(a), the dotted line represents off-resonance scattered-light background. Fluctuations of background level with input-signal wavelength and detailed alignment appears to be responsible for the dips in observed output power below the off-resonance background level. The minimum insertion loss for the data of Fig. 8(b) is 10.8 dB, again including coupling loss. In the limit of low reflectivity for both gratings, the peak reflected powers of Fig. 8(b) and Fig. 8(a) should be in the ratio of $(0.33)^2$:1 or -9.6 dB. The measured contrast is less than this because the fully written first-order grating [Fig. 8(a)] is in the regime of moderately high reflectivity. In Fig. 8(c), we superimpose the output power profiles of the fully (solid curve) and partially written HBRs and normalize them to the same peak value. Presented in this way, one can clearly see small sidelobes in the measured output power of the partially written HBR at approximately 150 and 250 μm. The spatial location of the observed sidelobes agrees well with the location expected on the basis of the simulation shown in Fig. 6(d). The side lobe magnitude observed is somewhat larger than the $\approx 10^{-5}$ expected on the basis of Fig. 6 extrapolated to the case of 13 305 diffractive contours. The 40-dB contrast observed between the primary output peak and the grayscale sidelobe is, however, fully adequate for many applications. It should be noted that the simulated and fabricated partially written HBRs have not been optimized for sidelobe suppression. The angular pattern shifts and variation in θ_k may be deterministically controlled during design for more effective sidelobe suppression.

In Fig. 9, we compare spectra and reflected power levels of a first-order, partially written, 0.33-fill-factor HBR (dotted line) and a third-order, fully written, 1.0-fill-factor HBR (solid line). The partially written HBR has 33 percent of each contour

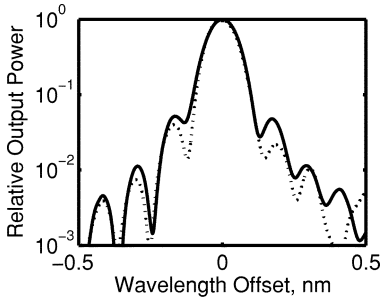

Fig. 9. Superimposed reflection spectra of a 0.33 grayscale first-order HBR (dotted line) and a fully written third-order HBR. Spectral widths and peak reflectivity are essentially identical confirming the ability of partial-fill grayscale to control reflection amplitude.

written as described above. Note that the written diffractive contour fraction of 33% is maintained uniformly throughout the device. This type of uniform diffractive contour apodization is expected to reduce the overall reflected field strength while maintaining the spectral transfer function of the unapodized structure. For the spectral measurement, a die equipped with input and output channel waveguides was employed. Actual spectra are obtained by scanning a fixed-polarization test laser across the HBR reflective peak. In Fig. 9, all data are multiplied by the same constant factor so that the peak of the solid curve equates to unity. Differences between the solid and dotted line are preserved. It is seen that the first-order 0.33-written HBR and the third-order 1.0-written HBR have essentially identical reflectivity. This result is fully consistent with our premise that fill-factor equates to diffractive amplitude. Applying the grayscale concept to Fig. 9, we expect that the reflected field should scale as the total number of diffractive contours in the HBR multiplied by the fill-factor (reflective amplitude) of the contours. Thus, we expect the first-order 0.33-written HBR and third-order 1.0-written HBR to have the same reflectivity—as indeed they do.

From Fig. 9, we also see that the reflection spectra of the partially written and completely written HBRs are virtually identical as one would expect for first- and third-order HBRs of the same length whose only difference is the reflective amplitude of diffractive elements. To facilitate comparison of the spectra, they have been horizontally shifted to a common wavelength origin. The actual peak reflection wavelengths of the two HBRs are 1530.93 and 1530.75 nm for the first-order 0.33-filled and third-order 1.0-filled HBR, respectively.

Here, we have studied the use of partial diffractive contour scribing as a means of achieving precise reflective amplitude control in distributed 2-D diffractive structures. We find that the spatial imaging and spectral properties of HBR devices are left intact through use of partial contour scribing provided that simple sidelobe suppression design features are incorporated. We find that overall reflective strength scales as expected with the fraction of diffractive contours scribed with trenches. Demonstration of these performance factors is crucial in the implementation of effective grayscale methods for general apodization of 2-D spectral devices. A remaining factor to be studied is the ability to adjust separations between contours in a heavily apodized structure to compensate for small effective

refractive index changes introduced in the process of changing contour fill factors. We point out that partial-fill grayscale can be implemented in slightly modified form in channel waveguide gratings. We also note that partial-fill grayscale is fully consistent with stamping-based replication of HBR and other distributed reflector devices.

It should be noted that partial scribing of HBR diffractive contours is also useful as a means to overlay multiple HBRs on the same spatial region. In the overlay process, a single photolithographic step creating the diffractive contours of all HBRs may be employed. As the HBR count increases, overlap of diffractive contours eventually leads to a uniform etch of the waveguide surface. If the diffractive contours are partially written, overlap of diffractive contours can be minimized, or, via explicit design constraint, completely eliminated.

C. Intrinsic Polarization-Insensitivity of HBRs

Polarization-insensitive spectral filtering is a highly desirable feature for many photonics applications. In the present section, we present results indicating that the tested HBR structures themselves are largely insensitive to input polarization changes. On the other hand, residual birefringence in the slab waveguide can give rise to significant polarization-dependent bandpass shifts. An alternate form of the HBR is proposed that utilizes channel waveguides rather than slab waveguides. The former are known via arrayed-waveguide grating work to support low birefringence.

In Fig. 10, we display HBR bandpass functions observed using different input polarizations for three different HBR device types produced on a single wafer. Fig. 10(a)–(c) corresponds, respectively, to first-, second-, and third-order HBRs. The solid (dashed) lines correspond to TE (TM) input polarization. For all three HBRs, the TM and TE bandpass functions are shifted by approximately 0.8 nm, corresponding to a fractional resonance wavelength difference $\Delta\lambda/\lambda$, 5×10^{-4}. We note that the polarization-dependent bandpass shifts seen in fabricated HBRs depend on waveguide dopants and detailed wafer anneal conditions. The shifts shown in Fig. 10 are among the largest observed. If the HBR structures themselves were responsible for the polarization-dependent bandpass shifts, one would expect a decrease in the shift with increasing HBR order. Higher-order HBRs contain more space without corrugation, i.e., trenches, where propagation and, hence, resonance is controlled by intrinsic slab waveguide properties. The absence of a dependence of the bandpass shift with HBR order suggests that the shifts arise from residual waveguide birefringence rather than as a feature of intrinsic HBR operation.

To test this premise, we performed an independent measurement of the slab waveguide birefringence. Linearly polarized light, whose polarization direction made an angle of 45° relative to the slab waveguide plane, was injected to a region of HBR free slab waveguide. Power transmitted through a 20-mm-long slab waveguide section and an analyzer polarizer oriented parallel to the input polarization was recorded. Slab birefringence produces power oscillation with injected wavelength. From the observed oscillation period, we estimate the slab birefringence $\Delta n/n$ to be 7×10^{-4}, which is consistent in magnitude with the birefringence needed to introduce the observed polarization-mediated shifts in HBR bandpass functions.

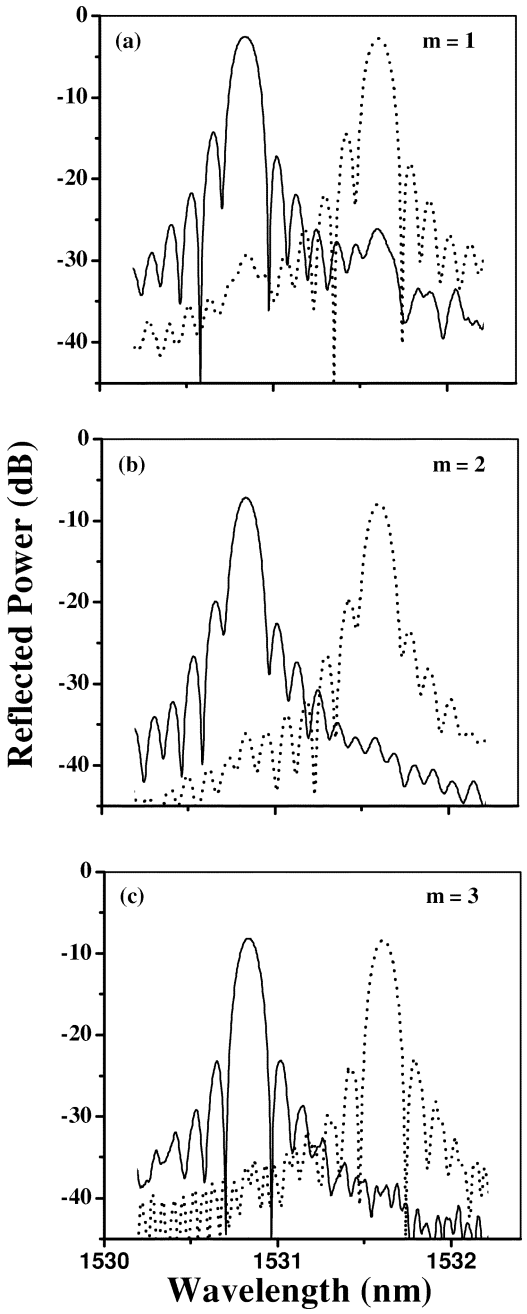

Fig. 10. HBR spectral transfer functions for TE (solid lines) and TM (dashed lines) input polarizations. Graphs (a)–(c) correspond to HBRs operating in first-, second-, and third-order, respectively.

The observed birefringence is a known problem of the silica-on silicon platform and is attributed to strain in the glass layers due to the different thermal expansion coefficients of the glass and silicon [26]. A number of methods have been proposed and demonstrated to overcome this problem, among them the introduction of strain-relieving grooves [27], which have made possible nearly birefringence-free silica-on-silicon channel waveguides and the demonstration of essentially polarization-independent 1-D Bragg reflectors [26]. Intriguingly, the HBR approach demonstrated in this paper is fully consistent

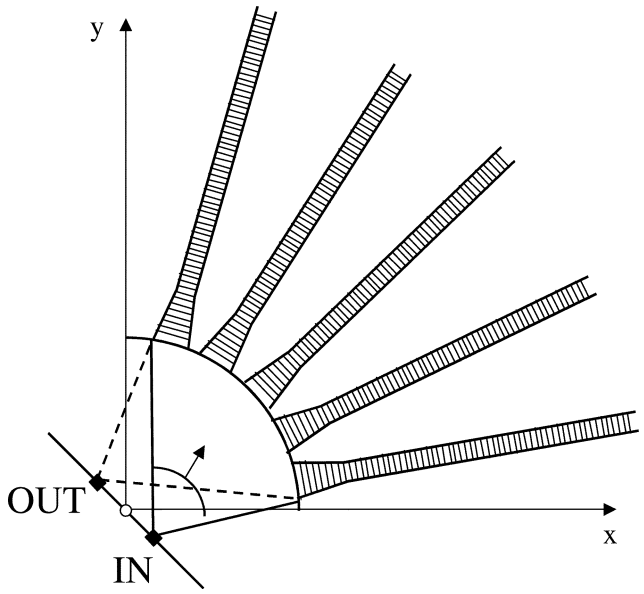

Fig. 11. Channel-waveguide-sampled 2-D planar hologram.

with implementation in a channel-waveguide-based format that provides all the functionality of the purely slab-waveguide HBR while at the same time being capable of harnessing all the birefringence mitigation techniques developed for channel waveguides.

Fig. 11 illustrates the channel-waveguide HBR concept, which can be briefly characterized as a channel-waveguide sampled holographic Bragg reflector. An array of channel waveguides radiate out from the HBR center of curvature branching out from an open slab waveguide region, which ends just prior to the first diffractive contour of a normal slab HBR. The channel waveguides contain segments of the diffractive contours that would have been in the full slab waveguide. The spectral filtering and wavefront focusing properties of the channel waveguide HBR are largely unmodified from the slab HBR case. In the regions between the channel waveguides core material may be removed via etching so as to implement birefringence-reducing strain-relieving grooves.

In more general cases, the arrangement of channel waveguide outputs shown in Fig. 11 forms a fully integrated planar diffraction grating wherein the amplitude, phase and output bandpass of each grating aperture, i.e., channel waveguide output, is determined by the grating contained within the respective guide. Since the latter are completely independent of each other, powerful phase and amplitude manipulation of the diffracted field at the waveguide output can be obtained via lithographic control of the amplitude and phase of the individual channel-contained gratings. This approach constitutes a very powerful means for both spectral and spatial tailoring of the hologram output diffraction pattern. We note that outputs of the waveguide array can be recombined to collect signals not resonant with the gratings.

When the device output port location OUT is chosen to coincide with the zeroth-order of the channel-manifold grating the polarization-dependence of the device spectral transfer function at the output port is dependent for the most part on the polarization properties of the 1-D Bragg reflectors and substantial reduction of polarization-dependence may thus be obtained by use of birefringence-free channel waveguides. Note that the device of Fig. 11 may exhibit higher grating orders, e.g., arising from regularly angular spacing of waveguides. These may provide additional device output ports. Alternatively, irregular angular placement or increased wave guide output apertures may be used to suppress higher grating orders.

IV. Conclusion

In summary, we have examined the feasibility of several aspects important to the implementation of HBRs as photonic devices. We demonstrated that standard photolithographic fabrication techniques can provide coherent holographic devices of about a centimeter in length whose performance is only limited by basic Fourier-transform and diffraction theory. We found that partial diffractive contour writing, i.e., effective grayscale apodization, provides for precise reflective amplitude control in distributed 2-D diffractive structures while leaving the spatial imaging and spectral properties of HBR devices intact. This demonstration is crucial for implementing effective grayscale methods for general apodization of 2-D spectral devices.

We find that polarization-dependent bandpass shifts observed can be attributed to residual slab waveguide birefringence and not to intrinsic performance properties of HBR structures themselves. We describe a “channel-waveguide-sampled” HBR concept that allows the many imaging and focusing properties of HBR devices to be realized while at the same time allowing birefringence mitigation approaches developed for channel waveguides to be employed.

We envision HBRs as providing the basis of a fully 2-D “photonic fabric” that can spectrally process and spatially route freely intersecting optical data streams from one active circuit element to another without constraining wire-like channel waveguides. The HBR platform provides many optics-on-a-chip functionalities. When several planar holographic structures are overlaid, stacked or interleaved a filtering device connecting one input port to several output ports may be generated. Such a multiport device constitutes a demultiplexer, when different output ports are associated with different wavelengths, represents a multiport spectral comparator, when constituent gratings are programmed with specific spectral signatures, i.e., of chemical or biological agents, or yields a multiport packet decoder for temporal pattern recognition/generation, when individual gratings operate as optical cross correlators. Additional applications include add-drop multiplication, spectral LED slicing or on-chip laser wavelength locking. When implemented in semiconductor materials, the planar HBR approach has the potential to integrated both active and passive optical components with electronic processing in a single substrate—a pathway to highly integrated ultracompact photonic circuits.

References

[1] T. W. Mossberg, “Planar holographic optical processing devices,” *Opt. Lett.*, vol. 26, pp. 414–416, 2001.

[2] ——, “Lithographic holography in planar waveguides,” *SPIE Holography Newsletter*, vol. 12, 2001.

[3] C. Greiner, D. Iazikov, and T. W. Mossberg, "Lithographically scribed, focusing, planar holographic Bragg reflector with 17-GHz passband and 0.3 cm^2 footprint," in *Optical Fiber Communication Conf.*, Atlanta, GA, Mar. 23–28, 2003, post-deadline paper PD31.
[4] T. Erdogan, "Fiber grating spectra," *J. Lightwave Technol.*, vol. 15, pp. 1277–1294, 1997.
[5] T. Komukai, K. Tamura, and M. Nakazawa, "An efficient 0.04-nm apodized fiber Bragg grating and its application to narrow-band spectral filtering," *IEEE Photon. Technol. Lett.*, vol. 9, pp. 934–936, July 1997.
[6] C. Marra, A. Nirmalathas, D. Novak, C. Lim, L. Reekie, J. A. Besley, C. Weeks, and N. Baker, "Wavelength-interleaved OADM's incorporating optimized multiple phase-shifted FBG's for fiber-radio systems," *J. Lightwave Technol.*, vol. 21, pp. 32–39, 2003.
[7] A. Grunnet-Jepsen, A. E. Johnson, E. S. Maniloff, T. W. Mossberg, M. J. Munroe, and J. N. Sweetser, "Fiber Bragg grating based spectral encoder/decoder for lightwave CDMA," *Electron. Lett.*, vol. 35, pp. 1096–1097, 1999.
[8] D. Wiesmann, C. David, R. Germann, D. Erni, and G. L. Bona, "Apodized surface-corrugated gratings with varying duty cycles," *IEEE Photon. Technol. Lett.*, vol. 12, pp. 639–641, June 2000.
[9] D. Wiesmann, R. Germann, G. L. Bona, C. David, D. Erni, and H. Jackel, "Add-drop filter based on apodized surface-corrugated gratings," *J. Opt. Soc. Amer. B*, vol. 20, pp. 417–423, 2003.
[10] J. Liu, Y.-L. Lam, Y.-C. Chan, Y. Zhou, B. S. Ooi, G. Tan, and J. Yao, "Embossed Bragg gratings on organically modified silane waveguides in InP," *Appl. Opt.*, vol. 39, pp. 4942–4945, 2000.
[11] R. Waldhäusl, B. Schnabel, P. Dannberg, E.-B. Kley, A. Bräuer, and W. Karthe, "Efficient coupling into polymer waveguides by gratings," *Appl. Opt.*, vol. 36, pp. 9383–9390, 1997.
[12] M. T. Gale, "Replication technology for holograms and diffractive optical elements," *J. Imag. Sci. Technol.*, vol. 41, pp. 211–220, 1997.
[13] J. Wang, S. Schablitsky, Z. Yu, W. Wu, and S. Y. Chou, "Fabrication of a new broadband waveguide polarizer with a double-layer 190 nm period metal-gratings using nanoimprint lithography," *J. Vac. Sci. Technol. B*, vol. 17, pp. 2957–2960, 1999.
[14] J. L. Rebola and A. V. T. Cartaxo, "Performance optimization of Gaussian apodized fiber Bragg grating filters in WDM systems," *J. Lightwave Technol.*, vol. 8, pp. 1537–1544, 2002.
[15] A. Carballar, M. A. Muriel, and J. Azana, "Fiber grating filter for WDM systems: an improved design," *IEEE Photon. Technol. Lett.*, vol. 11, pp. 694–696, June 1999.
[16] C. Marra, A. Nirmalathas, D. Novak, C. Lim, L. Reekie, J. A. Besley, C. Weeks, and N. Baker, "Wavelength-interleaved OADM's incorporating optimized multiple phase-shifted FBG's for fiber-radio systems," *J. Lightwave Technol.*, vol. 21, pp. 32–39, 2003.
[17] K. O. Hill, B. Malo, F. Bilodeau, S. Theriault, D. C. Johnson, and J. Albert, "Variable-spectral-response optical waveguide Bragg grating filters for optical signal processing," *Opt. Lett.*, vol. 20, pp. 1438–1440, 1995.
[18] Y. Shibata, T. Tamamura, S. Oku, and Y. Kondo, "Coupling coefficient modulation of waveguide grating using sampled grating," *IEEE Photon. Tech. Lett.*, vol. 6, pp. 1222–1224, Oct. 1994.
[19] T. Erdogan and D. G. Hall, "Circularly symmetric distributed feedback laser: coupled mode treatment of TE vector fields," *J. Quantum Electron.*, vol. 28, pp. 612–623, 1992.
[20] R. H. Jordan, D. G. Hall, O. King, G. Wicks, and S. Rishton, "Lasing behavior of circular grating surface emitting semiconductor lasers," *J. Opt. Soc. Amer. B*, vol. 14, pp. 449–453, 1997.
[21] S. Kristjansson, N. Eriksson, A. Larsson, R. S. Penner, and M. Fallahi, "Observation of stable cylindrical modes in electrically pumped circular grating-coupled surface-emitting lasers," *Appl. Opt.*, vol. 39, pp. 1946–1953, 2000.
[22] M. Li, B. S. Luo, C. P. Grover, Y. Feng, and H. C. Liu, "Waveguide grating coupler with a tailored spectral response based on a computer-generated waveguide hologram," *Opt. Lett.*, vol. 24, pp. 655–657, 1999.
[23] J. Backlund, J. Bengtsson, C. Carlstrom, and A. Larsson, "Input waveguide grating couplers designed for a desired wavelength and polarization response," *Appl. Opt.*, vol. 41, pp. 2818–2825, 2002.
[24] C. H. Henry, R. F. Kazarinov, Y. Shani, R. C. Kistler, V. Pol, and K. J. Orlowsky, "Four-channel wavelength division multiplexers and bandpass filters based on elliptical Bragg reflectors," *J. Lightwave Technol.*, vol. 8, pp. 748–755, 1990.
[25] V. Yankov, S. Babin, I. Ivonin, A. Goltsov, A. Morozov, L. Polonskiy, M. Spector, A. Talapov, E.-B. Kley, and H. Schmidt, "Multiwavelength Bragg gratings and their application to optical MUX/DEMUX devices," *IEEE Photon. Technol. Lett.*, vol. 12, pp. 410–412, Mar. 2003.
[26] R. Adar, C. H. Henry, R. H. Kistler, and R. F. Kazarinov, "Polarization independent narrow band Bragg reflection gratings made with silica-on-silicon waveguides," *Appl. Phys. Lett.*, vol. 60, pp. 1779–1781, 1992.
[27] Y. Inoue, K. Katoh, and M. Kawachi, "Polarization sensitivity of a silica waveguide thermooptic phase shifter for planar lightwave circuits," *IEEE Photon. Technol. Lett.*, vol. 4, pp. 36–38, 1992.

C. Greiner (M'02) received the M.A. and Ph.D. degrees in optical physics from the University of Oregon, Eugene, in 1995 and 2002, respectively.

Since 2002, he has been a Senior Scientist with LightSmyth Technologies, Eugene, OR. Presently, his main research interests concern the development of integrated photonic components based on planar holographic Bragg reflectors.

Dr. Greiner is a Member of the American Physical Society, the German Physical Society, the Optical Society of America (OSA), and the International Society for Optical Enginers (SPIE).

D. Iazikov (M'03) was born in St. Petersburg, Russia, in 1971. He received the B.S. and M.S. degrees in applied optics from Moscow University of Physics and Technology, Moscow, Russia, in 1990 and 1993, respectively.

He has been involved in the development of optical components and systems since 1990 and has recently held positions as Design Authority at JDS Uniphase's thin-film-filter-based wide-band wavelength-division-multiplexing group and as Technical Lead for arrayed-waveguide grating and optical add/drop multiplexing development at Zenastra Photonics. Since joining LightSmyth Technologies, Eugene, OR, as a Senior Scientist in 2002, he has been engaged in the design and characterization of holographic Bragg reflector-enabled planar lightwave circuits.

T. W. Mossberg (M'96) received the B.A. degree from the University of Chicago, Chicago, IL, in 1973 and the M.A. and Ph.D. degrees from Columbia University, New York, in 1975 and 1978, respectively.

He has served on the faculties of Columbia University, Harvard University, and the University of Oregon. During the mid-1990s, he co-founded Templex Technologies and is currently Chief Technology Officer of LightSmyth Technology, Eugene, OR, specializing in the design and fabrication of planar holographic optical devices and distributed photonic circuits. He has published approximately 140 refereed technical articles treating optics and physics.

Dr. Mossberg is a Fellow of the American Physical Society and the Optical Society of America (OSA).